



Trisodium citrate assisted synthesis of hierarchical NiO nanospheres with improved supercapacitor performance

Dandan Han^{a,b}, Pengcheng Xu^b, Xiaoyan Jing^{a,c}, Jun Wang^{a,c,*}, Piaoping Yang^a, Qihui Shen^b, Jingyuan Liu^a, Dalei Song^a, Zan Gao^a, Milin Zhang^{a,c}

^a Key Laboratory of Superlight Materials and Surface Technology, Ministry of Education, Harbin Engineering University, Harbin 150001, PR China

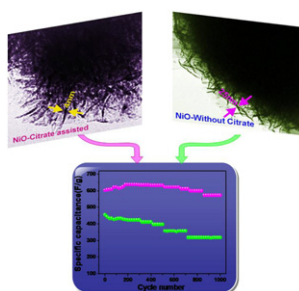
^b College of Chemistry and Pharmaceutical Engineering, Jilin Institute of Chemical Technology, Jilin 132022, PR China

^c Institute of Advanced Marine Materials, Harbin Engineering University, Harbin 150001, PR China

HIGHLIGHTS

- ▶ NiO samples were synthesized using a facile trisodium citrate assisted route.
- ▶ Citrate positioned in the precursor interlayer to control the morphology and size.
- ▶ Citrate-assisted NiO showed higher specific capacitance and lower ESR.
- ▶ Citrate-assisted NiO exhibited good cycling stability and capacitance retention.

GRAPHICAL ABSTRACT



ARTICLE INFO

Article history:

Received 26 October 2012

Received in revised form

25 January 2013

Accepted 29 January 2013

Available online 9 February 2013

Keywords:

Hierarchical nickel oxide
Trisodium citrate
Porous nanosheet
Electrochemical performance

ABSTRACT

Hierarchical NiO nanospheres composed of porous nanosheets are prepared by a facile trisodium citrate assisted precipitation route followed by a calcination process. Effects of the trisodium citrate on the microstructure and electrochemical performances of NiO nanospheres are systematically investigated. The XRD, SEM, TEM, BET, and TG analyses show that the key point of the successful realization is that the citrate positioned in the precursor α -Ni(OH)₂ layer, which can prevent the restacking of α -Ni(OH)₂ sheets, yielding better crystallinity, high surface area (182 m² g⁻¹) as well as pore volume (0.15 cm³ g⁻¹) and hierarchical porous ball-like morphology of NiO nanospheres by the calcination of the precursor. Electrochemical results show that the hierarchically porous NiO obtained with trisodium citrate assisted route exhibits high rate charge–discharge performance (463 F g⁻¹ at 4.5 A g⁻¹), longer cyclic stability (95% capacitance remained after 1000 charge–discharge cycles at 0.5 A g⁻¹) as compared to the NiO prepared in the absence of sodium citrate (182 F g⁻¹ at 4.5 A g⁻¹; 70% capacitance retention after 1000 charge–discharge cycles at 0.5 A g⁻¹). Further, due to facile mass transfer in the perfectly porous nanosheet, the citrate-assisted NiO show lower equivalent series resistance as revealed from the impedance studies.

Crown Copyright © 2013 Published by Elsevier B.V. All rights reserved.

* Corresponding author. College of Materials Science and Chemical Engineering, Harbin Engineering University, Harbin 150001, Heilongjiang province, PR China. Tel.: +86 451 8251 3026; fax: +86 451 8253 3026.

E-mail addresses: luckhan2006@163.com (D. Han), xupengcheng911@163.com (P. Xu), jingxiaoyan@hrbeu.edu.cn (X. Jing), junwang@hrbeu.edu.cn (J. Wang), yangpiaoping@hrbeu.edu.cn (P. Yang), qihuishen@126.com (Q. Shen), liujingyuan1004@hrbeu.edu.cn (J. Liu), sdl031012@163.com (D. Song), 308294430@qq.com (Z. Gao), zhangmilin@hrbeu.edu.cn (M. Zhang).

1. Introduction

The greater role of porous structured materials in dealing with the challenges in new sustainable and renewable energy is receiving wide attention [1–4]. Especially, metal oxides with infinite variety of hierarchically multimodal pore size distributions exhibit indispensable surface properties for energy harvesting,

conversion, and storage [5]. In the recent past, fundamental aspects of synthesis, processing, and control of multiscale oxide structures have been achieved for more efficient energy conversion and storage applications [5–7]. In this context, the role of high surface area, appropriate narrow pore size distribution (2–5 nm), optimal particle dimension and architecture, and the controlled pore channels are highly emphasized.

Electrochemical capacitors (ECs) represent an emerging energy storage technology that offers high power density, long cycling life and fast recharge ability. ECs store energy using either ion adsorption (electrochemical double layer capacitors) or fast surface redox reactions (pseudo-capacitors) [8,9]. Redox-based ECs materials have shown the potential to combine the high energy density of conventional batteries and the high power capabilities of electrostatic capacitors [10]. Transition metal oxides such as RuO_2 [11–14], MnO_2 [15–18], Co_3O_4 [19–21] and NiO [22–24] are considered as the most promising pseudocapacitor candidate materials due to their high capacitances with several times larger than carbonaceous materials. ECs based on RuO_2 are capable of delivering specific capacitance ranging from 720 to 860 F g^{-1} (for a single electrode system) [12]. However, apart from being toxic, RuO_2 is quite expensive for extensive commercial applications. Therefore, great efforts have been devoted to searching for inexpensive alternative materials with good capacitive characteristics similar to RuO_2 .

Among the explored systems, NiO is of particular interest owing to its easy availability, cost effectiveness, and good pseudocapacitive behavior [25,26]. Several different synthesis approaches have been employed to tune the size, shape, and hence the properties of such materials. Commonly, layered nickel hydroxide ($\text{Ni}(\text{OH})_2$) with various morphologies can be conveniently synthesized in solutions of $\text{Ni}(\text{II})$ by a chemical precipitation method, while NiO can be conveniently prepared by thermal decomposition of $\text{Ni}(\text{OH})_2$. It has been known that two polymorphic forms of layered nickel hydroxide ($\text{Ni}(\text{OH})_2$) exist: the α - and β -phases. A main feature differentiation between these phases is the presence of intercalated species (water and/or anions) within the interlayer galleries of α - $\text{Ni}(\text{OH})_2$. β - $\text{Ni}(\text{OH})_2$ has a brucite-like structure ($a = 3.12 \text{ \AA}$, $c = 4.6 \text{ \AA}$; JCPDS Card No. 14-0117) comprised of perfectly stacked $\text{Ni}(\text{OH})_2$ layers which do not contain water or any charge-balancing anions between its layers. α - $\text{Ni}(\text{OH})_2$ have a structure similar to LDHs [27], on the other hand, is a hydrotalcite-like structure (JCPDS Card No. 38-0715) comprised of randomly stacked $\text{Ni}(\text{OH})_{2-x}$ layers along the c -axis intercalated with water or anions. The basal spacing (from 31.7 to 7.5 \AA) and morphologies of α - $\text{Ni}(\text{OH})_2$ can be controlled by adjusting the species intercalated in the interlayer galleries [28]. Lee et al. [29] synthesized hierarchical microspheres α - $\text{Ni}(\text{OH})_2$ nanosheets intercalated with desired anionic species (Cl^- , NO_3^- , OAc^- , and SO_4^{2-}) showed different specific capacitance with varies size of the intercalated anions. Ida et al. [30] reported the synthesis of layered nickel hydroxide intercalated with dodecyl sulfate, and then successfully eliminated dodecyl sulfate molecules between the $\text{Ni}(\text{OH})_2$ layers, resulting in the formation of hexagonal α - $\text{Ni}(\text{OH})_2$ nanosheets that are potentially useful in ultrathin film devices.

Citrate/citrate acid as a shape-directing has been extensively applied for the synthesis of diverse metal oxide nanostructures. Xing et al. [31] synthesized mesoporous β - $\text{Ni}(\text{OH})_2$ and NiO nanospheres with ammonia and citrate by a hydrothermal process heated at 100°C for 24 h showed the specific capacitance 290 F g^{-1} . Nathan and co-workers [32] have prepared nanoscale bulk powders NiO with citrate acid as a chelating agent, but the electrodes only provide a specific capacitance of 200 F g^{-1} at scan rate 5 mV s^{-1} . In this context, there is few literature about citrate ion as a layer intercalated agent to control the morphology and size of the

α - $\text{Ni}(\text{OH})_2$ precursor growth of hierarchically porous NiO by a facile methods with high specific capacitance and excellent electrochemical properties.

In this study, we employed a quite fast, facile, energy-saving and environmental friendly precipitation route to prepare lamellar precursor α - $\text{Ni}(\text{OH})_2$ with citrate ion intercalated. Finally, the hierarchical NiO with porous nanosheet is obtained by the gas impulse generated from burning the citrate by a further calcination process. As a result, the unique structure NiO shows excellent electrochemical properties, high rate capacitance and good cycling stability for supercapacitor applications.

2. Experimental section

2.1. Synthesis procedure

All the chemicals are of analytical grade and were used without further purification. In a typical process, 15 mmol $\text{Ni}(\text{SO}_4)_2 \cdot 6\text{H}_2\text{O}$, 15 mmol Hexamethylenetetramine ($\text{C}_6\text{H}_{12}\text{N}_4$), and 4.08 mmol trisodium citrate dihydrate ($\text{C}_6\text{H}_5\text{Na}_3\text{O}_7 \cdot 2\text{H}_2\text{O}$) were dissolved in 100 mL aqueous solution, and the solution was heated at 90°C for 2 h with the sealed flask. After the solution was cooled naturally to room temperature, the green precipitate was separated, washed with double distilled water several times, and dried in a vacuum at 80°C for 4 h. Finally, the sample was obtained by calcination in flowing air at a heating ramp of 5°C min^{-1} from room temperature to 300°C and kept at this temperature for 3 h, which is denoted as NiO-Cit . A comparative experiment was carried out in a similar manner in the absence of trisodium citrate.

2.2. Characterization

X-ray diffraction (XRD) measurement was examined on a Rigaku D/max TTR-III diffractometer using $\text{Cu K}\alpha$ radiation ($\lambda = 0.15405 \text{ nm}$). Thermogravimetric analyses (TG) were performed at a heating rate of $10^\circ\text{C min}^{-1}$ in air on a thermal analyzer (TA SDT-Q600, American). Fourier transform infrared spectroscopy (FT-IR) was measured on a Perkin–Elmer 580B IR spectrophotometer. The morphologies of the samples were inspected on a scanning electron microscope (SEM, S-4800, Japan HITACHI). Transmission electron microscopy (TEM) micrographs were performed on an FEI Tecnai G^2 20 S-TWIN transmission electron microscope with a field emission gun operating at 200 kV. N_2 adsorption/desorption was performed on a Micromeritics ASAP 2010 instrument. The specific surface area was calculated by the Brunauer–Emmett–Teller (BET) method.

2.3. Preparation of electrodes and electrochemical characterization

To evaluate the electrochemical properties of the NiO microstructures, working electrodes were prepared as follows. The as-prepared materials, graphite, acetylene black, and poly(tetrafluoroethylene) (PTFE) were mixed in a mass ratio of 75:10:10:5 and dispersed in ethanol to produce a homogeneous paste. Graphite, acetylene black and PTFE were used as the conductive agent and binder, respectively. Then the mixture was coated onto the nickel foam substrate ($1 \text{ cm}^2 \times 1 \text{ cm}^2$) with a spatula. Finally, the fabricated electrodes were dried at 60°C for 1 day in a vacuum oven. The mass of active materials in working electrode was 0.01 g. Cyclic voltammetry (CV), chronopotentiometry (CP), and electrochemical impedance spectroscopy (EIS) measurements were carried out using conventional three-electrode configuration on a CHI 660 D electrochemical workstation. The Ni foam coated with NiO was used as the working electrode, and platinum foil ($1 \text{ cm}^2 \times 1 \text{ cm}^2$) and a saturated calomel electrode (SCE) were used

as the counter and reference electrodes. All the experiments were carried out using freshly prepared 5.0 M aqueous KOH electrolyte in double distilled water. The EIS measurements were carried out in the frequency range from 100 kHz to 0.05 Hz at open circuit potential with an ac perturbation of 5 mV.

3. Results and discussion

3.1. Material characterization

XRD patterns of α -Ni(OH)₂ precursors prepared with and without sodium citrate are shown in Fig. 1a. Regardless of the experimental route, intense layer diffraction peak (001) is observed in the low angle range ($2\theta < 20^\circ$), which can be assigned to the (003) plane of α -Ni(OH)₂ (JCPDS no. 38-0715), providing clear evidence of a layered structure [33,34]. Nevertheless, the peak of α -Ni(OH)₂ with citrate located in the interlayer space shifts to a lower angle (i. e. larger d -spacing) compared to α -Ni(OH)₂ prepared in the absence of sodium citrate, suggesting that intercalated citrate anions between interlayer layers enlarge the interlayer spacing. The basal spacing of α -Ni(OH)₂-Cit calculated based on the (003) reflection was 0.99 nm, which is larger than that of α -Ni(OH)₂ (0.78 nm) synthesized without trisodium citrate and similar to those of other α -Ni(OH)₂ with acetate or sulfate intercalated [29]. Furthermore, two broad and asymmetric peaks are observed at about 34.0° and 60.2° , corresponding to nonbasal spacing, which are present in turbostratic materials. Turbostratic disorder can be explained by a stacking order of brucite-like structures parallel to and equidistant along the c -axis of the hexagonal structure but randomly twists relative to each other, which agree well with other α -Ni(OH)₂ samples [28,29].

In the typical TG curves, the two kind of precursors display two-step weight loss at about 60 and 300 °C (Fig. 1b). The first weight loss may arise from the removal of intercalated water or

absorbed water, and the second weight loss is due to the decomposition of intercalated anions and dehydration of Ni(OH)₂. The clear difference of the weight loss in the two temperature regions should correspond to the intercalated anions. The total weight loss of 65.3% for α -Ni(OH)₂-Cit has larger mass loss than that of α -Ni(OH)₂ without citrate additives (33.6%), which does not have any citrate anions but sulfate and water molecules [35]. In conclusion, the difference in weight loss is due to the additives of citrate intercalated between Ni(OH)₂ layers which makes the precursor samples undergo decomposition via two different routes.

More concrete proof for the anionic species in the interlayer of α -Ni(OH)₂-Cit can be given by the FT-IR spectra, as depicted in Fig. 1c. The broad band around 3440 cm^{-1} is assigned to a $\nu_{\text{O-H}}$ stretching band, and confirms the presence of a hydroxyl group of the brucite structure of α -Ni(OH)₂ phase [36]. The band at 2963 cm^{-1} is attributed to a C-H stretching vibration of HMT molecules [37]. In addition, the two weak bands at 1146 and 1067 cm^{-1} are characteristics of C-N vibration, indicating that HMT molecules are positioned in the interlayer space [35,37]. A strong band at 1400 and 1580 cm^{-1} in Fig. 1c,a can be assigned to the C=O vibration of $\text{C}_6\text{H}_5\text{O}_3^{2-}$ located in the interlamellar space of the α -Ni(OH)₂ [38]. Furthermore, the vibration bands at 1128 and 1045 cm^{-1} in Fig. 1c,b correspond to the vibration of SO_4^{2-} [39]. In conclusion, it is confirmed that citrate anions are successfully inserted into the α -Ni(OH)₂ interlayer.

XRD patterns of NiO-Cit prepared with and without the assistance of sodium citrate are given in Fig. 1d. Obviously, the diffraction peaks are directly indexed to pure NiO phase (JCPDS no. 47-1049), indicating that the temperature of 300 °C is sufficient to completely convert α -Ni(OH)₂ to NiO. The diffraction peak intensity changes due to the size variation of the product. XRD diffractions of NiO-Cit are more intense compared to that of NiO formed in the absence of citrate, indicating the high crystallinity.

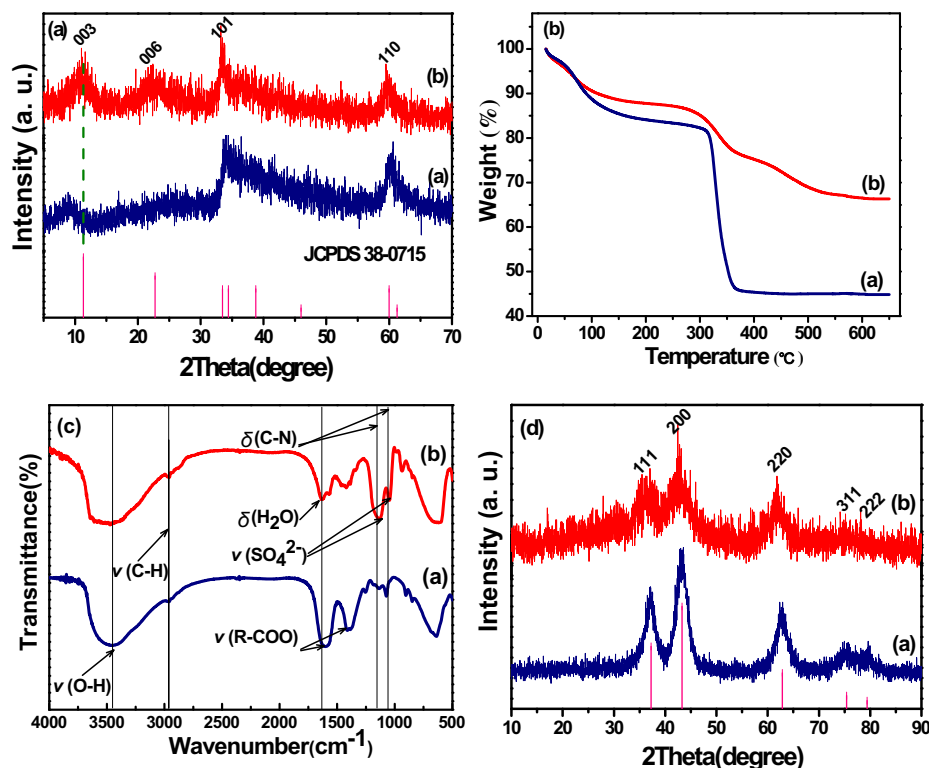


Fig. 1. (a) XRD patterns, (b) TG profiles, (c) FT-IR spectra of α -Ni(OH)₂ precursors and (d) XRD patterns of NiO samples prepared with (a) and without (b) sodium citrate.

The morphologies of the hierarchical NiO–Cit were examined by FESEM and TEM measurements. When citrate is present, agglomerated flower like regular structures congregated on randomly arranged nanosize flakes are found, which mass with each other leaving plenty of porous channels between the spheres (Fig. 2a,b). The texture of the nanospheres is further identified by the TEM images. As shown, numerous thin nanosheets with irregular shapes aggregate and form dandelion like hierarchical spheres with a diameter of 100–250 nm. The thickness of the nanosheets is approximately 2–5 nm (Fig. 2c). Interestingly, NiO–Cit (Fig. 2d) clearly shows porous structure with slit-shaped pores on the flakes, which may be formed by the removal of citrate during the calcination process. Moreover, the nanosheets overlap with each other to afford a three-dimensional conducting network, which might have high surface area, and consequently could provide high specific capacitance due to easy access of the active species in the redox process at the interface of the electrode. The representative high-resolution TEM image taken from the NiO nanosheet was shown in Fig. 2e. The distinct lattice fringe with an interplanar distance of 0.26 nm was observed, corresponding to the spacing of the (111) planes of NiO crystals (Fig. 2f).

To study the effect of citrate on the morphology, the NiO sample in the absence of citrate was performed under the same conditions. In the FESEM images (Fig. 3a,b), microspheres based on the nanosheets with varying size from 1 to 5 μm are observed. It should be pointed that the porous structure pores on the flakes are not observed. Additionally, the nanosheets of NiO–Cit synthesized

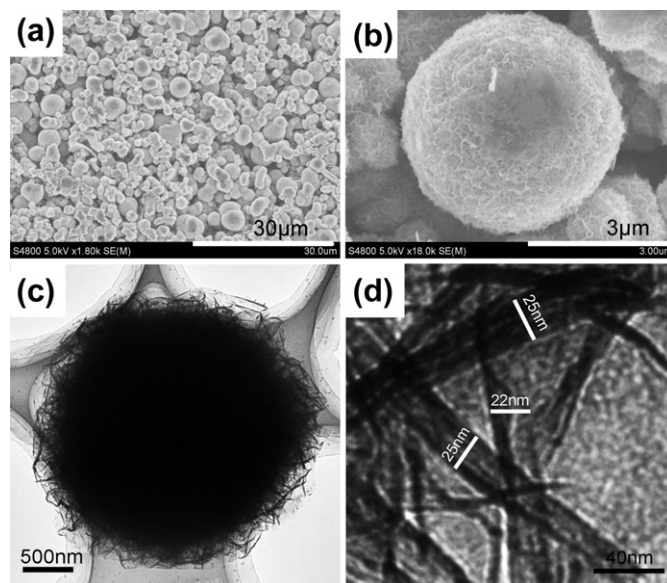
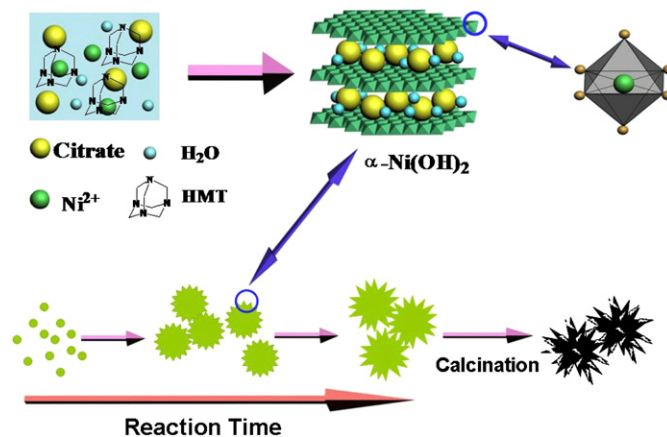


Fig. 3. (a) Low- and (b) high-resolution FESEM images and (c) low- and (d) high-resolution HRTEM images of NiO prepared in the absence of sodium citrate.

from the addition of citrate are much more thinner and homogeneous than those of sample prepared without citrate (Fig. 3c,d). It is clear that the hierarchical NiO based on porous nanosheet are formed only in the presence of citrate. Theoretical studies show that the generation of these types of irregular as well as highly ordered surface structures is mostly due to the self-assembly process during structural growth anisotropic Ostwald ripening [40,41]. As shown in Scheme 1, during the initial nucleation process, hexamethylenetetramine ($\text{C}_6\text{H}_{12}\text{N}_4$) works as a pH buffer by slowly releasing OH^- ions through thermal decomposition. Obviously, $\text{C}_6\text{H}_5\text{Na}_3\text{O}_7$ does not react with any compound but ionized to form bulky $\text{C}_6\text{H}_5\text{O}_3^{3-}$ in the HMT solution [42]. Then, $\alpha\text{-Ni}(\text{OH})_2$ with a hydrotalcite-like structure with citrate intercalated is formed by Ni centers coordinated in an octahedral arrangement with OH^- groups. The two-dimensional sheets stack by hydrogen bonding between the hydroxyl groups of adjacent sheets [43]. However, $\text{Ni}(\text{OH})_2$ layers intercalated with citrate should have much weaker hydrogen bonding, yielding thinner and more flexible sheets. By the effect of oriented attachment, the $\alpha\text{-Ni}(\text{OH})_2$ nanospheres intercalated citrate were formed which had smaller size and transformed to NiO with almost porous nanostructure via



Scheme 1. Schematic illustration of the morphology evolution of NiO–Cit.

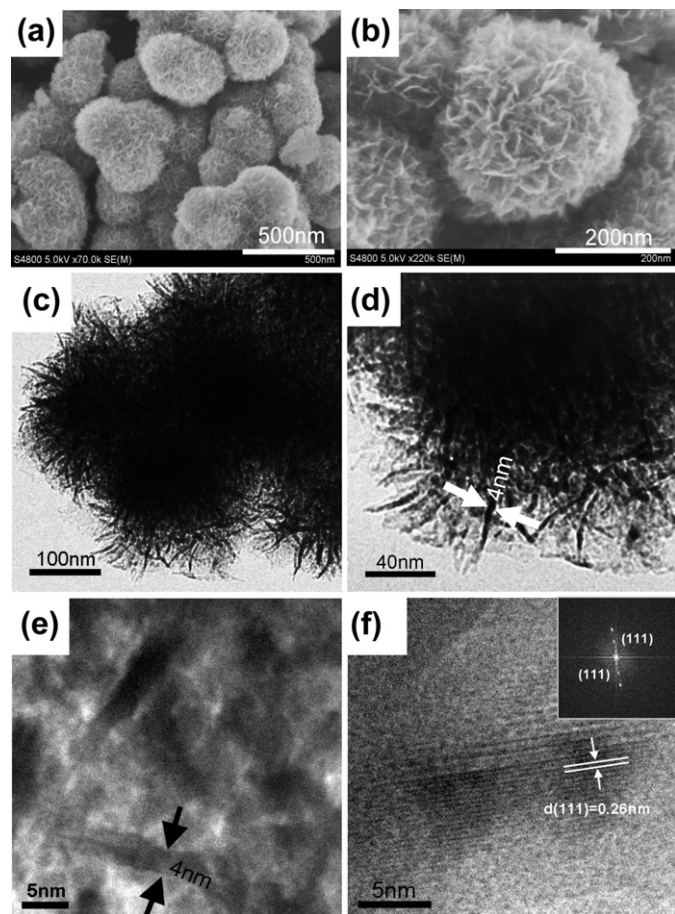


Fig. 2. (a) Low- and (b) high-resolution FESEM images of NiO–Cit sample; (c) low- and (d, e, and f) high-resolution HRTEM images of NiO–Cit sample and the insert is corresponding FFT pattern.

calcination. This phenomenon has been reported for other intercalated anions of α -Ni(OH)₂ sample [29]. Morphologies of NiO microstructures are different from reported other NiO [13,17,18,20]. During the calcination, the hierarchical morphologies of NiO did not change, but the slit-shaped pores on the flakes are formed by the gas impulse arising from the calcination of the intercalated citrate, which effectively enhance their surface area.

The hierarchical porosity feature of NiO–Cit is further confirmed by nitrogen adsorption/desorption isotherms with corresponding pore size distributions, as shown in Fig. 4a. According to the IUPAC classification, the isotherms can be classified as type IV isotherm [44]. The measured BET specific surface area and pore volume of NiO–Cit is 182 m² g^{−1} and 0.15 cm³ g^{−1}. Moreover, the pore size distribution is narrow with a single modal centered at 2.1 nm. Such small pores are presumably generated from pore opening when the citrate or intercalated water is removed between Ni(OH)₂ layers. In Fig. 4b, the pore size distribution maxima of the NiO synthesized in the absence of trisodium citrate are centered at 50 nm. In addition, the surface area and pore volume of the sample reduce to 47 m² g^{−1} and 0.04 cm³ g^{−1}, respectively. The dramatically reduced specific surface area is due to the large particle size or small pore walls. In conclusion, NiO–Cit has a uniform framework with both a regular mesoporous size distribution and the optimal pore size range of 2–5 nm, which should be favorable to improve the capacitance behavior of an electroactive material due to unhindered diffusion and accession of electrolyte ions into the inner space/matrix [45].

3.2. Electrochemical characterization

To explore the potential application of the as-synthesized hierarchical NiO–Cit microspheres, the sample was fabricated as supercapacitor electrodes and characterized by CV, EIS, and galvanostatic charge/discharge measurements.

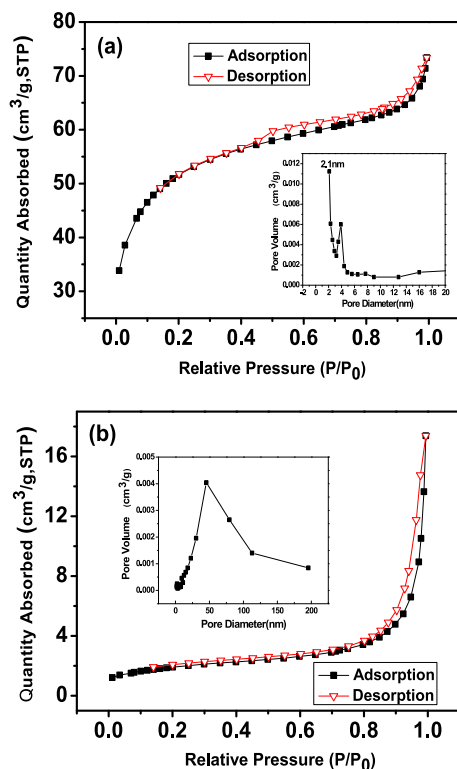
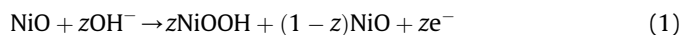


Fig. 4. N₂ adsorption/desorption isotherms and pore size distributions (insets) of NiO–Cit (a) and citrate free sample (b).

The CV patterns of NiO electrodes with and without sodium citrate assisted route at scan rate of 10 mV s^{−1} in 5 M KOH solution are shown in Fig. 5. The individual NiO–Cit and NiO without citrate assisted sample electrodes were subjected to one time stabilization/activation by repeated CV cycles (30 numbers) at sweep rates of 50 mV s^{−1} in the similar potential range, before performing the CV experiments for accessing the electrochemical performance. The CV patterns of both the samples show identical shapes, which are typical of pseudocapacitance behavior due to occurrence of faradaic redox reactions in the system. The respective anodic and cathodic peaks at the positive and negative current density correspond to following charge–discharge phenomena [46–48].



The potential difference ($\Delta E_{a,c}$) between the anodic and cathodic peaks is used as a measure of the reversibility of the electrochemical redox reaction: the higher the reversibility, the smaller the $\Delta E_{a,c}$ [49]. Table 1 shows that $\Delta E_{a,c}$ of NiO–Cit sample is smaller than NiO in the absence of sodium citrate, indicating good reversibility of the electrochemical redox reactions for the porous sample. In addition, the difference ($\Delta E_{oe,a}$) between the oxygen evolution potential (E_{oe}) and E_a is another important indicator for raising the oxygen evolution over potential [49]. The larger the value is, the better the charge efficiency of the active material is. That is, a large difference between E_{oe} and E_a allows fully oxidation of Ni (II) to Ni (III) before the evolution of the oxygen. The potential difference ($\Delta E_{oe,a}$) was 130 mV for the NiO–Cit electrode, higher than that of NiO without citrate assisted. Moreover, a higher specific capacitance of the NiO in the case of sodium citrate aided process is exhibited by the larger area of CV curve, which is associated with referred slit-shaped surface morphology [50].

The CV responses of the NiO–Cit and NiO without citrate assisted samples carried out at different scan rates (2–50 mV s^{−1}) in a fixed potential range of 0–0.4 V in aqueous 5 M KOH electrolyte are shown in Fig. 6a and b, respectively. The CV profiles of NiO samples at different scan rates almost have obvious symmetric anodic and cathodic peaks, which reveals that the redox process occurs in NiO associated with active component diffusion controlled [47]. There are small changes in the shape of the CV curves observed with scan rate in Fig. 6a. A slightly positive shift of the oxidation peak potential and a negative shift of the reduction peak potential as compared to the counterpart without citrate even at higher scan rates, which is solely due to less polarization resistance. The linear response of the peak current intensity with the scan rate (the insets of Fig. 6a) is also an indication of the fast electronic and

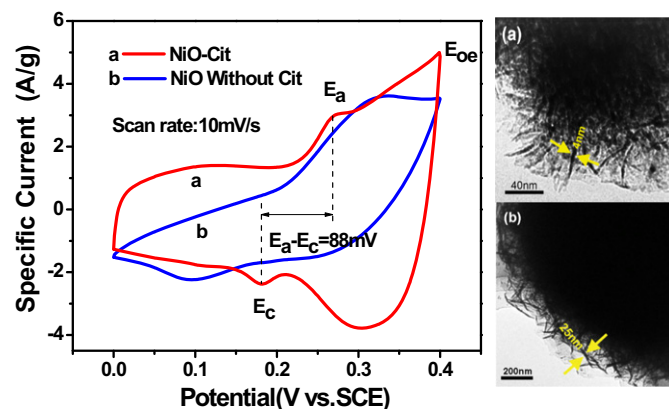


Fig. 5. Comparison of cyclic voltammograms and TEM images of (a) NiO–Cit and (b) NiO without citrate at a scan rate of 10 mV s^{−1}.

Table 1
Electrochemical parameters from CVs of the samples^a.

Electrodes	E_a (mV)	E_c (mV)	$\Delta E_{a,c}$ (mV)	E_{oe} (mV)	$\Delta E_{oe,a}$ (mV)
NiO–Cit	270	182	88	400	130
NiO (no Cit)	319	96	223	400	81

^a ΔE_a and E_c are defined as the anodic (oxidation) peak potential and cathodic (reduction) peak potential, respectively and E_{oe} is defined as the oxygen evolution potential.

ionic transport rates [18,51]. The specific capacitance (C_s , F g^{−1}) values at different scan rates (ν , V s^{−1}) in the CV measurements were calculated using the following equation [40,52]:

$$C_s = \frac{1}{\nu w(\Delta V)} \int_{V_a}^{V_c} i dV \quad (2)$$

where ΔV (V) is the applied potential window (V_a to V_c) and w (g) is the weight of the active material. At potential scan rates of 2–50 mV s^{−1}, the specific capacitance values for NiO–Cit sample are found to be 563–346 F g^{−1}. Similarly, at the same scan rates the specific capacitance values for NiO without citrate-assisted sample are in the range of 482–105 F g^{−1}. The CV data show that there is a continuous decrease in the specific capacitance values with increase in potential scan rate (Fig. 6c). This is an important aspect of porous materials where the resistance of the pores plays a significant role during charge storage process. The pore structure of an electrode material can influence the distributed resistance inside the pores which further controls the nature of response current (capacitive or resistive) during CV cycling. An electrode material with suitable pore structure (easy channeling of ions) contributes positively toward the capacitive nature of response

current and charge storage efficiency. As in the NiO–Cit sample the pores are more regular, the ionic mobility is less hindered, which minimize resistance inside the pores and result in better capacitance retention at higher redox reaction conditions. This is reflected in the higher specific capacitance value and ~39% capacitance loss with increase in the scan rate from 2 to 50 mV s^{−1}. However, during similar CV scans, NiO without citrate assisted sample shows lower specific capacitance value and suffers ~78% capacitance loss with increase in the scan rate from 2 to 50 mV s^{−1}. This demonstrates the higher current response of NiO–Cit sample, which is due to the high accessibility of OH[−] ions on the surface consisting of numerous nanochannels.

Since long cycle-life is the most important criterion for a supercapacitor, an endurance test of NiO–Cit sample was conducted using CV 200 times between 0.0 and 0.4 V at a nominal scan rate of 50 mV s^{−1} shown in Fig. 6d. It is found that the curves almost overlapped with each other between 10 and 200 CV cycles for stabilization. Moreover, the current response almost remained constant and the peak potential position changed very little, which indicating good cycling stability for the sodium citrate assisted obtained NiO.

Supercapacitors being power devices, lower resistance of the electrode materials is electrochemically preferred for better applicability. For further understanding, the impedance of NiO with and without sodium citrate, and the NiO–Cit sample after 200th cycles was measured in the frequency range of 100–0.05 kHz at open circuit potential with an ac perturbation of 5 mV (Fig. 7). The measured impedance spectra was analyzed using the CNLS fitting method based on the equivalent circuit [52], which is given in the inset of Fig. 7. It is found that two major characteristic features in the high and low frequency regions are attributed to various resistance phenomena during different interfacial processes in Faradaic reactions. R_s and R_{ct} are solution and charge-transfer

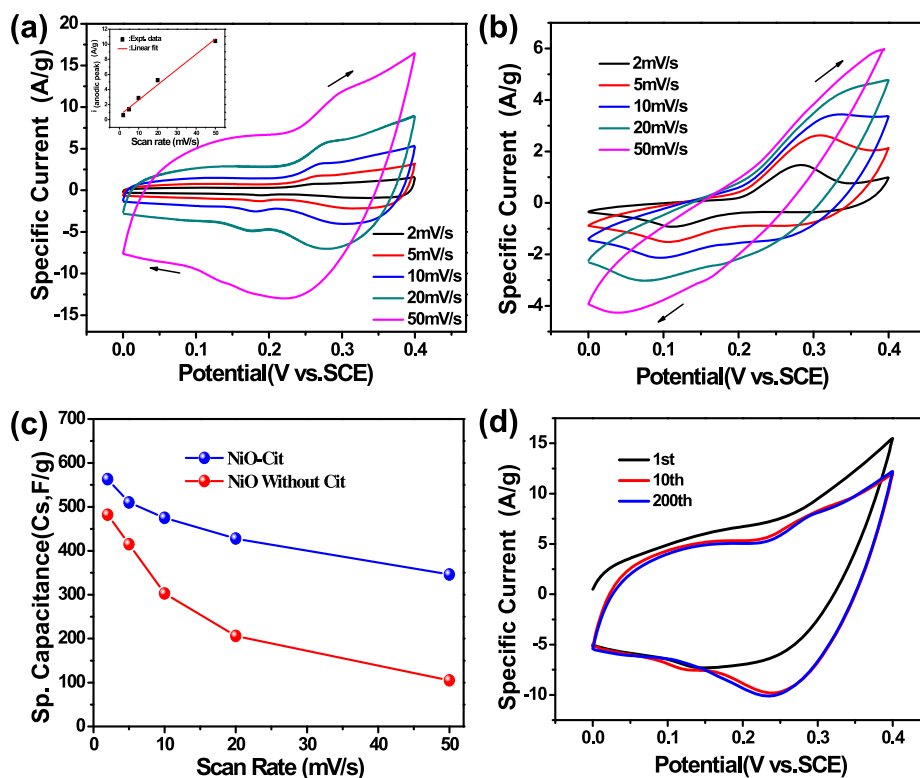


Fig. 6. CV curves of NiO–Cit prepared with (a) and without (b) sodium citrate at different scan rates; specific capacitance as a function of scan rate of NiO–Cit (c) and CV curves of NiO–Cit at the 1st, 10th and 200th at a scan rate of 50 mV s^{−1} (d). The inset of (a) shows the linearity of anodic current density with scan rate.

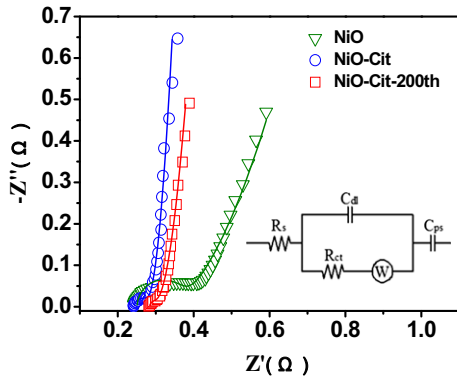


Fig. 7. Nyquist plots of experimental impedance data (scattering dot) and fitting results (solid line) for NiO–Cit before and after 200 charge–discharge cycles and comparative samples. Inset shows the electrical equivalent circuit used for fitting impedance spectra.

Table 2

The calculated values of R_s , C_{dl} , R_{ct} , Z_W and C_{ps} through CNLS fitting of the experimental impedance spectra based on the proposed equivalent circuit in Fig. 7.

	R_s (Ω)	C_{dl} (F)	R_{ct} (Ω)	Z_W (Ω)	C_{ps} (F)
NiO (no Cit)	0.2511	0.0005347	0.1164	0.5782	0.001545
NiO–Cit	0.2435	0.0005747	0.0003302	0.8990	0.01281
NiO–Cit-200th	0.2840	0.4634	0.00001828	15.1	6.921

resistances, respectively. C_{dl} and C_{ps} in the circuit represents double layer and pseudocapacitance, respectively. The slope of the 45° portion of the curve is called the Warburg resistance (W), which is a result of the frequency dependence of ion diffusion/transport in the electrolyte [53]. The values of R_s , R_{ct} , C_{dl} , C_{ps} and W calculated

from CNLS fitting of the experimental impedance spectra are presented in Table 2. Obviously, the NiO–Cit after 200th cycling has the least charge-transfer resistance (R_{ct}) because of the increase in electroactive surface area of the electrode material. The electroactive surface area increased with increasing specific surface area and electrical conductivity. The larger the electroactive surface area, the lower the charge-transfer resistance [54]. However, there is a major difference about the ion diffusion/transport in the electrolyte (W). After 200 cycles, the ion diffusion or transport for the capacitive electrode is increased. As the diffusion resistance (W) is obviously affected by the porous structure of the active materials, increase in the diffusion resistance (W) may be caused by the loss of perfect pore size distribution (2–5 nm) [55].

To further understand the high rate capability of the samples, the charge/discharge measurements at different current densities were recorded. Fig. 8a,b display the charge–discharge curves of NiO–Cit and NiO without citrate samples at current densities of 0.5, 1.5, and 4.5 A g^{−1}. Specific capacitance values of NiO–Cit and NiO without citrate samples have been calculated from the voltage time measurements at applied current densities (i), active mass of the sample (m), and the discharge slope of the chronopotentiometric discharge curve (dV/dt), using the equation [56]:

$$C_s = \frac{i}{[m(dV/dt)]} \quad (3)$$

The specific capacitance values of NiO–Cit sample at scan rates of 0.5, 1.5, and 4.5 A g^{−1} are found to be 603, 544, and 463 F g^{−1}, respectively. Similarly, the specific capacitance values for NiO sample without citrate at the same scan rates are found to be 455, 288, and 182 F g^{−1}, respectively. It is clear that under a relatively large current density of 4.5 A g^{−1}, nearly 77%, and 40% of the initial value was remained for NiO–Cit and NiO without citrate electrode, respectively. It indicates that the enhanced rate capability

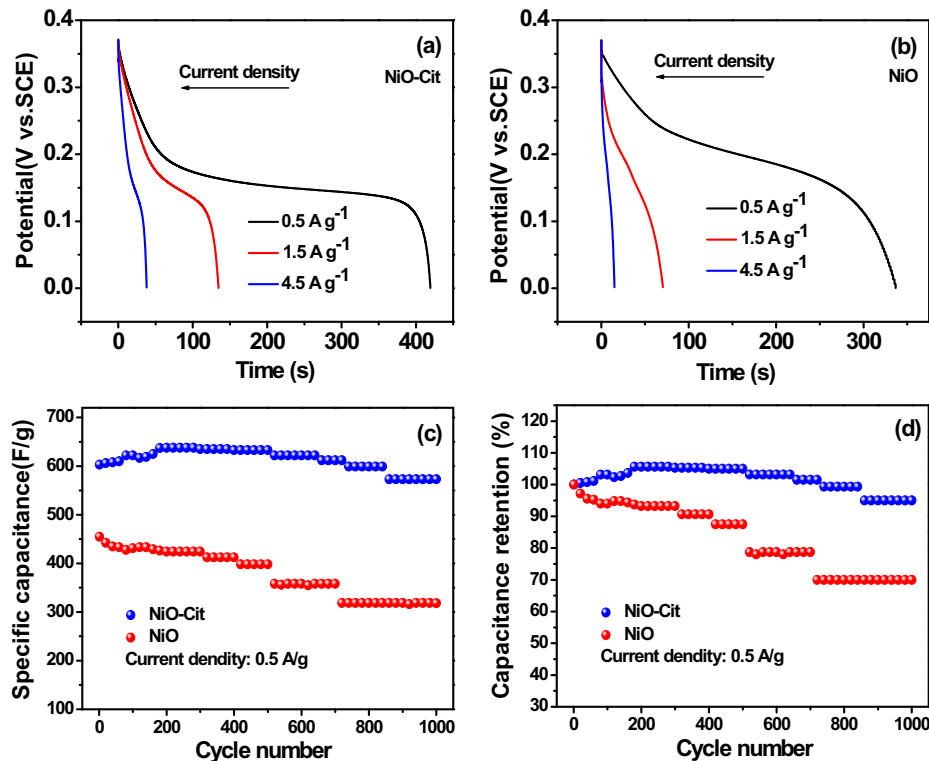


Fig. 8. Discharge curve of (a) NiO–Cit and (b) NiO samples at different current densities; cyclic performance and % capacitance retention of those electrodes (c and d) performed at 0.5 A g^{−1} in 5.0 M KOH solution.

capacitance of NiO–Cit sample is a combined contribution of high porosity with superior pore–channel structure and large internal accessible surface which in turn facilitate the electrolyte penetration into the sample matrix, decrease the ion diffusion resistance and enhance the electroactive surface utilization during the redox process [57]. Besides, the nanosize channels in the rippled shape surface of NiO–Cit sample alleviate ion hopping between the neighboring surface sites, thereby easing the ion diffusion and increasing the dynamics of charge propagation during the charge storage process [58]. Further, numerous nanochannels and higher pore volume of the sample act as “ion-buffering reservoirs” which reduce the mean free path of the anions and facilitate faster ionic and electronic kinetics, thus maximizing the reversible insertion/de-insertion reactions. The NiO without citrate sample, due to lower surface area, pore volume and agglomerated thick flake like structure, contains lower number of electroactive surface sites, and the irregular pores as well as disoriented pore walls induce random scattering of OH^- ions, which enhance the diffusion resistance and decrease the kinetics of these ions inside the sample.

As higher life-cycle stability is very crucial for an electrode material to be practically used in electrochemical capacitor, the samples for both the method were tested for 1000 galvanostatic charge–discharge cycles at the current density of 0.5 A g^{-1} (Fig. 8c), with corresponding capacitance retention plots shown in Fig. 8d. Noticeably, the degradation of the specific capacitance of NiO–Cit is 5% after 1000 cycles, which is lower than the counterpart without citrate (30% capacitance degradation). Small increase in specific capacitance values for initial 200 charge–discharge cycles is observed for NiO–Cit electrode, which is ascribed to the surface activation (pore opening) of the porous structures. As reported recently on hierarchical porous pine-cone structure [24], the reason for the unique property of the porous NiO material is the fibrous porous network, which can shorten the diffusion path length of OH^- ions for the reversible redox process by acting as an “ion-buffering reservoir”. The interfacial area between the electrode and the electrolyte is larger due to the assembled nanofibers on porous NiO surface (Fig. 2) which results in higher diffusion rates and significantly faster electronic kinetics. The porous nanosheet structure improves the solid-state diffusion, intercalation/de-intercalation of OH^- ions, and the overall cyclic stability of NiO.

4. Conclusions

In summary, the NiO nanospheres with hierarchical nano-structures based on slit-shaped pores were successfully prepared via a simple and rapid alkaline precipitation method with the assistance of trisodium citrate. The surface morphology, structure, and capacitive behaviors of the NiO nanospheres were well investigated. The intercalated citrate can successfully locate in the layer space of the as-synthesized $\alpha\text{-Ni}(\text{OH})_2$, subsequent calcination yields hierarchical NiO with porous structure. Taking advantage of these characteristics, NiO–Cit nanospheres improves the capacitance of the electrode, and showed good retention for more than 1000 cycles in a cycling test with lower charge-transfer resistance, suggesting its high promising prospective for SCs.

Acknowledgments

This work was supported by Special Innovation Talents of Harbin Science and Technology (2011RFQXG016), Fundamental Research Funds of the Central University (HEUCFZ), Key Program of the Natural Science Foundation of Heilongjiang Province (ZD201219), Program of International S&T Cooperation special project (S2013ZR0649), Special Innovation Talents of Harbin Science and Technology (2012RFXXG104), 12th Five-Year Plan in

Science and Technology of the Education Department of Jilin Province (2012290) and “ChunMiao” talents special project in Science and Technology of the Education Department of Jilin Province.

References

- [1] J. Lee, J. Kim, T. Hyeon, *Adv. Mater.* 18 (2006) 2073–2094.
- [2] C.X. Guo, F.P. Hu, X.W. Lou, C.M. Li, *J. Power Sources* 195 (2010) 4090–4097.
- [3] C.X. Guo, C.M. Li, *Energy Environ. Sci.* 4 (2011) 4504–4507.
- [4] J. Baxter, Z. Bian, G. Chen, D. Danielson, M. Dresselhaus, A.G. Fedorov, T.S. Fisher, C.W. Jones, E. Maginn, U. Kortshagen, A. Manthiram, A. Nozik, D.R. Rolison, T. Sands, Li. Shi, D. Shollh, Y. Wu, *Energy Environ. Sci.* 2 (2009) 559–563.
- [5] Y.Q. Zhang, X.H. Xia, J.P. Tu, Y.J. Mai, S.J. Shi, X.L. Wang, C.D. Gu, *J. Power Sources* 199 (2012) 413–417.
- [6] J. Liu, G. Cao, Z. Yang, D. Wang, D. Dubois, X. Zhou, G.L. Graff, L.R. Pederson, J.G. Zhang, *Chem. Sus Chem.* 1 (2008) 676–697.
- [7] G.R. Patzke, Y. Zhou, R. Kontic, F. Conrad, *Angew. Chem. Int. Ed.* 50 (2011) 826–859.
- [8] S.B. Ma, K.W. Nam, W.S. Yoon, X.Q. Yang, K.Y. Ahn, K.H. Oh, K.B. Kim, *Electrochim. Commun.* 9 (2007) 2807–2811.
- [9] S.J. Bao, C.M. Li, C.X. Guo, Y. Qiao, *J. Power Sources* 180 (2008) 676–681.
- [10] X. Zhao, B.M. Sanchez, P.J. Dobson, P.S. Grant, *Nanoscale* 3 (2011) 839–855.
- [11] C.C. Hu, K.H. Chang, M.C. Lin, Y.T. Wu, *Nano Lett.* 6 (2006) 2690–2695.
- [12] J.T. Zhang, J.Z. Ma, L.L. Zhang, P.Z. Guo, J.W. Jiang, X.S. Zhao, *J. Phys. Chem. C* 114 (2010) 13608–13613.
- [13] A. Devadas, S. Baranton, T.W. Napporn, C. Coutanceau, *J. Power Sources* 196 (2011) 4044–4053.
- [14] R.R. Bi, X.L. Wu, F.F. Cao, L.Y. Jiang, Y.G. Guo, L.J. Wan, *J. Phys. Chem. C* 114 (2010) 2448–2451.
- [15] H.S. Nam, J.S. Kwon, K.M. Kim, J.M. Ko, J.D. Kim, *Electrochim. Acta* 55 (2010) 7443–7446.
- [16] Q. Lu, Y.K. Zhou, *J. Power Sources* 196 (2011) 4088–4094.
- [17] P. Yu, X. Zhang, D.L. Wang, L. Wang, Y.W. Ma, *Cryst. Growth Des.* 9 (2009) 528–533.
- [18] R. Amade, E. Jover, B. Caglar, T. Mutlu, E. Bertran, *J. Power Sources* 196 (2011) 5779–5783.
- [19] T. Zhu, J.S. Chen, X.W. Lou, *J. Mater. Chem.* 20 (2010) 7015–7020.
- [20] X.H. Xia, J.P. Tu, X.L. Wang, C.D. Gu, X.B. Zhao, *Chem. Commun.* 47 (2011) 5786–5788.
- [21] R. Tummala, R.K. Guduru, P.S. Mohanty, *J. Power Sources* 209 (2012) 44–51.
- [22] X.H. Xia, J.P. Tu, Y.J. Mai, X.L. Wang, C.D. Gu, X.B. Zhao, *J. Mater. Chem.* 21 (2011) 9319–9325.
- [23] S.K. Meher, P. Justin, G. Ranga Rao, *Electrochim. Acta* 55 (2010) 8388–8396.
- [24] P. Justin, S.K. Meher, G. Ranga Rao, *J. Phys. Chem. C* 114 (2010) 5203–5210.
- [25] S.K. Meher, P. Justin, G. Ranga Rao, *Nanoscale* 3 (2011) 683–692.
- [26] C. Yuan, X. Zhang, L. Su, B. Gao, L. Shen, J. Mater. Chem. 19 (2009) 5772–5777.
- [27] P.V. Kamath, G. Helen Annal Therese, J. Gopalakrishnan, *J. Solid State Chem.* 128 (1997) 38–41.
- [28] J.W. Lee, T. Ahn, D. Soundararajan, J.M. Ko, J.D. Kim, *Chem. Commun.* 47 (2011) 6305–6307.
- [29] J.W. Lee, J.M. Ko, J.D. Kim, *J. Phys. Chem. C* 115 (2011) 19445–19454.
- [30] S. Ida, D. Shiga, M. Koinuma, Y. Matsumoto, *J. Am. Chem. Soc.* 130 (2008) 14038–14039.
- [31] S.T. Xing, Q. Wang, Z.C. Ma, Y.S. Wu, Y.Z. Gao, *Mater. Res. Bull.* 47 (2012) 2120–2125.
- [32] T. Nathan, A. Aziz, A.F. Noor, S.R.S. Prabaharan, *J. Solid State Electrochem* 12 (2008) 1003–1009.
- [33] B. Mavis, M. Akinc, *Chem. Mater.* 18 (2006) 5317–5325.
- [34] P. Jeevanandam, Y. Kolytyn, A. Gedanken, *Nano Lett.* 1 (2001) 263–266.
- [35] B.H. Liu, S.H. Yu, S.F. Chen, C.Y. Wu, *J. Phys. Chem. B* 110 (2006) 4039–4046.
- [36] Z.A. Hu, Y.L. Xie, Y.X. Wang, L.J. Xie, G.R. Fu, X.Q. Jin, Z.Y. Zhang, Y.Y. Yang, H.Y. Wu, *J. Phys. Chem. C* 113 (2009) 12502–12508.
- [37] M.Y. Cheng, B.J. Hwang, *J. Colloid Interface Sci.* 337 (2009) 265–271.
- [38] J. Zhang, F.Z. Zhang, L.L. Ren, D.G. Evans, X. Duan, *Mater. Chem. Phys.* 85 (2004) 207–214.
- [39] C. Nethravathi, N. Ravishanker, C. Shivakumara, M. Rajamathi, *J. Power Sources* 172 (2007) 970–974.
- [40] J.W. Lee, T. Ahn, J.H. Kim, J.M. Ko, J.D. Kim, *Electrochim. Acta* 56 (2011) 4849–4857.
- [41] Y.W. Chen, Q. Qiao, Y.C. Liu, G.L. Yang, *J. Phys. Chem. C* 113 (2009) 7497–7502.
- [42] S. Cho, J.W. Jang, S.H. Jung, B.R. Lee, E. Oh, K.H. Lee, *Langmuir* 25 (2009) 3825–3831.
- [43] G.G.C. Arizaga, K.G. Satyanarayana, F. Wypych, *Solid State Ionics* 178 (2007) 1143–1162.
- [44] M. Kruk, M. Jaroniec, *Chem. Mater.* 3 (2011) 3169–3183.
- [45] P. Simon, Y. Gogotsi, *Nat. Mater.* 7 (2008) 845–854.
- [46] B.R. Tao, J.A. Zhang, F.J. Miao, S.C. Hui, L.J. Wan, *Electrochim. Acta* 55 (2010) 5258–5262.
- [47] J.H. Kim, K. Zhu, Y.F. Yan, C.L. Perkins, A.J. Frank, *Nano Lett.* 10 (2010) 4099–4104.
- [48] D.C. Wang, W.B. Ni, H. Pang, Q.Y. Lu, Z.J. Huang, J. km, W. Zhao, *Electrochim. Acta* 55 (2010) 6830–6835.

- [49] J.W. Lang, L.B. Kong, W.J. Wu, Y.C. Luo, L. Kang, Chem. Commun. (2008) 4213–4215.
- [50] F.L. Zheng, G.R. Li, Y.N. Ou, Z.L. Wang, C.Y. Su, Y.X. Tong, Chem. Commun. 46 (2010) 5021–5023.
- [51] M. Hasan, M. Jamal, K.M. Razeeb, Electrochim. Acta 60 (2012) 193–200.
- [52] S.K. Meher, G. Ranga Rao, J. Phys. Chem. C 115 (2011) 15646–15654.
- [53] H.L. Li, S. Liua, C. Huang, Z. Zhou, Y.H. Li, D. Fang, Electrochim. Acta 58 (2011) 89–94.
- [54] H. Zhang, M. Zhang, Mater. Chem. Phys. 108 (2008) 184–187.
- [55] X.Y. Chen, C. Chen, Z.J. Zhang, D.H. Xie, X. Deng, J.W. Liu, J. Power Sources 230 (2013) 50–58.
- [56] X. Zhao, A. Wang, J. Yan, G. Sun, L. Sun, T. Zhang, Chem. Mater. 22 (2010) 5463–5473.
- [57] K. Byoungwoo, C. Gerbrand, Nature 458 (2009) 190–195.
- [58] S.K. Meher, G. Ranga Rao, J. Power Sources 215 (2012) 317–328.